Journal of Solid State Chemistry 277 (2019) 240–252

Contents lists available at ScienceDirect

Journal of Solid State Chemistry

journal homepage: www.elsevier.com/locate/jssc

Transformation mechanism of the pressure-induced $C2/c$-to-$P\bar{1}$ transition in ferrous sulfate monohydrate single crystals

J.M. Meusburger *, M. Ende, D. Talla, M. Wildner, R. Miletich

Institut für Mineralogie und Kristallographie, Universität Wien, Althanstrasse 14, A-1090 Wien, Austria

ARTICLE INFO

Keywords:
Ferrous sulfate monohydrate
High-pressure
Diamond-anvil cell
Ferroelastic phase transition
Kieserite-type structure

ABSTRACT

The kieserite-type ferrous sulfate $FeSO_4 \cdot H_2O$ has been studied up to pressures of 9.2 GPa by means of X-ray diffraction, Fourier-transform infrared spectroscopy and Raman spectroscopy. The monoclinic phase undergoes a ferroelastic pressure-induced phase transitions at $P_c = 6.154(1)$ GPa with the thermodynamic character being second order. The structure solution of the high-pressure polymorph revealed a purely displacive transition with the SO_4 and FeO_6 units remaining unchanged in their topology. Birch-Murnaghan equations of state were fitted to the unit-cell volume data thus yielding $V_0 = 365.23(30)$ Å^3, $K_0 = 45.2(2)$ GPa, $K' = 6.7(1)$ for the $C2/c$ phase and $V_0 = 369.86(46)$ Å^3, $K_0 = 38.5(6)$ GPa for the high-pressure $P\bar{1}$ polymorph with K' fixed to 5.4 as derived from normalized pressure-strain analysis. The analyses of the high-pressure spectra and the structure refinements reveal changes in the hydrogen-bonding system to be the responsible driving mechanism for the phase transition.

1. Introduction

Ferrous sulfate denotes a range of salts with the stoichiometric formula $FeSO_4 \cdot xH_2O$, representing compounds in various hydration states from anhydrous to fully hydrated heptahydrate ($0 \leq x \leq 7$). Although magnesium [1–5] and nickel [6] sulfates in higher hydration states have been identified, substitution with other divalent metals [7,8] and iron(II) in particular [9] appears to be rather limited. All ferrous iron sulfates dissolve in water giving the paramagnetic octahedral $[Fe(H_2O)_6]^{2+}$ hexaaquacomplex, of which the formation opens up a wide range of industrial applications. They encompass the use as a reducing agent, as a colorant (including e.g. the production of iron gall ink in ancient times) or uses in medicine against iron-deficiency anemia [10] or in horticulture to treat iron chlorosis [11]. Natural occurrences of hydrated ferrous sulfates are often bound to oxidation zones of sulfidic ore deposits, tailings, waste piles and associated acid mine drainage [12,13]. Hydrated sulfates including solid solutions of ferrous sulfates have been considered as potentially important constituents on the surface of Mars [14]. Moreover, sulfate minerals in $x = 6$, 7, 11 hydration states are proposed to be the dominant non-icy mineral phases on the surface of the outer three Galilean moons [15–17]. Incongruent melting has been observed for numerous hydrated sulfate minerals under pressure [3,4,18,19] and temperature [20–23] conditions relevant to the interior of giant icy satellites directing interest towards the high-pressure behaviour low-hydrated sulfate minerals such as monohydrates.

The crystalline monohydrate $FeSO_4 \cdot H_2O$, known as the mineral szomolnokite, was found to be isostructural to monoclinic $MgSO_4 \cdot H_2O$ (kieserite), of which the structure was determined by Leonhard & Weiss [24] in space-group $C2/c$. The kieserite structure type (Fig. 1) consists of corner sharing $[MO_4(H_2O)]^{6-}$ units, running parallel to the crystallographic c-axis and thus forming continuous chains//[001]. These chains share common oxygen atoms with the tetrahedral sulfate groups, thus providing the linkage to a three-dimensional heterodesmic framework. The structural topology shows distinct relations to those of titanite, amblygonite, caminite, lazulithe and lipscombite as discussed by Baur [26], Hawthorne et al. [27] and Zemann [28].

Investigations on series of synthetic representatives of kieserite-type sulfates [25] but also selenate analogues [29] revealed $C2/c$-endmembers for Mg, Fe, Ni, Co, Zn and Mn. The existence of continuous solid solutions was so far shown for the binary Mg-Co [30] and Mg–Fe systems [31], in both cases showing Vegard-type behaviour along the respective series. In the context of former systematic crystallochemical studies, $CdSO_4 \cdot H_2O$, known as the mineral voudourisite [32,33], was found to crystallize in $P2_1/n$ space-group symmetry [34], which can be attributed to a size mismatch of the Cd^{2+} cations located on the octahedral site. On the other hand, the lattice distortion and the associated deviation from aristotype $C2/c$ symmetry in $CuSO_4 \cdot H_2O$ (triclinic space group $P\bar{1}$) was explained by cooperative polyhedral distortion around the

* Corresponding author.
E-mail address: johannes.meusburger@gmail.com (J.M. Meusburger).

https://doi.org/10.1016/j.jssc.2019.06.004
Received 24 March 2019; Received in revised form 27 May 2019; Accepted 3 June 2019
Available online 5 June 2019

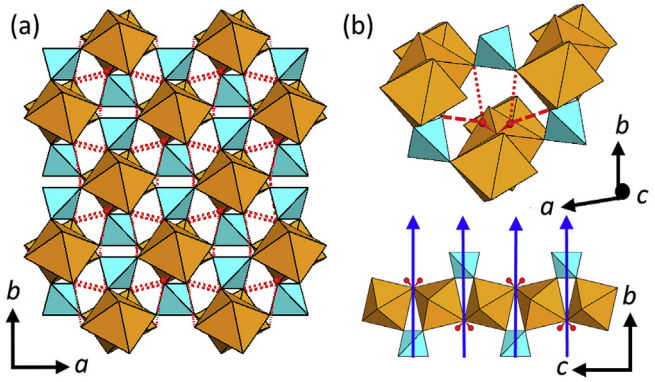

Fig. 1. (a) Projection of the kieserite-type *C*2/*c* structure of $FeSO_4{\cdot}H_2O$ along [001] and (b) details of the schematic hydrogen-bonding system with respect to the local twofold symmetry (FeO_6 octahedra: orange; SO_4 tetrahedra: turquoise; hydrogen atoms: red). Dashed lines represent short H···O2 contacts, dotted lines denote the H···O1 distance. Blue arrows indicate the axes of the rotational diads. Structure represented at ambient conditions as described by Wildner and Giester [25]. (For interpretation of the references to color in this figure legend, the reader is referred to the Web version of this article.)

Cu^{2+} cations due to the Jahn-Teller effects [35–37].

At ambient conditions hydrogen bonds exhibit linear geometry with two Ow···O2 bonds following the local two-fold symmetry of the water molecule [25,27,35]. Ow···O1 distances in kieserite-type compounds exceed the barely defined upper limit of hydrogen bonding [38]. But evidently at higher pressures the hydrogen bonding system reveals an increasing tendency towards bifurcation as the structure approaches a denser atomic configuration. The hydrogen-bonding system and in particular the role of acceptor atoms with respect to the existing local symmetry must be considered as the key to the structural stability of the aristotype *C*2/*c* structure. The existence of non-*C*2/*c* representatives is a clear indication of possible transformations into other polymorphs, in particular as the hydrogen-bonding network is different for these examples. Nevertheless, investigations of $FeSO_4{\cdot}H_2O$ at low-temperature conditions down to 113K by single crystal X-ray diffraction [31] and to even 7 K by Raman spectroscopy [39] did not provide any evidence for a structural phase transition. Considerations on the extent of structural changes imposed by variations of external conditions prompted us to consider investigations under high-pressure conditions, as any lattice change is expected to be much stronger as compared to that one originating from temperature variations.

For the present study we selected the ferrous endmember representative to be most suitable, because the critical cation size for Fe^{2+} ($r = 0.78$ Å) is intermediate between the smallest (0.69 Å, Ni^{2+}) and largest (0.83 Å, Mn^{2+}) values (ionic radii after [40]) within the series of various *C*2/*c*-representatives out of the $MSO_4{\cdot}H_2O$ phases. The objective of this work was therefore to investigate the structural evolution of synthetic $FeSO_4{\cdot}H_2O$ single crystals and their behaviour under hydrostatic pressure conditions. Using the diamond-anvil cell techniques, in-situ high-pressure investigations were carried out by means of X-ray diffraction and vibrational spectroscopy in order to record the structural evolution under pressure and track possible structural transitions.

2. Materials and methods

2.1. Synthesis of sample crystals

Single crystals of $FeSO_4{\cdot}H_2O$ were synthesized in Teflon-lined stainless steel hydrothermal autoclaves with an inner volume of ~55 cm^3 using the approach of Talla and Wildner [31]. The vessels were filled with ~6 g $FeSO_4{\cdot}7H_2O$ (*Alfa Aesar*). Problems regarding the oxidation from Fe^{2+} to Fe^{3+} in the hydrothermal solution leading to the formation of rhomboclase and other mixed Fe^{2+}/Fe^{3+} sulfates required redox buffering. Both attempts, either using a foil of metallic iron (dimensions $3 \times 10 \times 1$ mm) together with 25 cm^3 pure H_2SO_4 ($w = 0.73$), or the use of a mixture of 5 ml H_2SO_3 ($w = 0.06$) along with 20 cm^3 H_2SO_4 ($w = 0.73$) as solvent agent turned out to be successful routes for the synthesis of $FeSO_4{\cdot}H_2O$ as the single product. All chemicals specified above were of analytical purity. The filled vessels were heated for 24 h to 210 °C and cooled down at a controlled rate of −3 °C/h down to room temperature. The solid products were washed with distilled H_2O and 98% ethanol and finally dried at 65 °C. The phase type and purity were identified by Raman spectroscopy. Since the crystals were too large to be used for the pressure cell, they were gently crushed between two object slides. Due to the excellent cleavage parallel to (113) and (111), wafer-shaped crystal fragments were obtained, as morphologically predetermined by the cleavage directions.

2.2. High-pressure sample environment

Crystal fragments were loaded into *ETH-type* diamond-anvil cells (DAC) [41] equipped with either standard brilliant-cut diamond anvils or Boehler-Almax type anvils [42], each with a culet face of 600 µm in diameter. Type IIa anvils were used for infrared spectroscopy, while for all other techniques (XRD, Raman spectroscopy) type I diamonds were used. Stainless steel gaskets were pre-indented to ~100 µm and a ~250 µm diameter borehole was drilled by spark erosion in the center of the indentation. A water-free 4:1 methanol-ethanol mixture served as pressure-transmitting medium for XRD investigations, while in-situ vibrational spectroscopy was carried out on samples pressurized in cryogenically loaded argon. Both 4:1 methanol-ethanol [43,44] as well as argon [43,45] provide quasi-hydrostatic pressure distribution up to approximately 10 GPa and hence well above the maximum pressure reached in the experiments. Pressures were determined using the conventional quartz and ruby standards, following the calibration of Scheidl et al. [46] and Jacobson et al. [47], respectively. The estimated standard deviations (ESDs) of the *P* values obtained by the internal *P* standard quartz were determined by the ESDs of the measured *P*-dependent unit-cell volume. The ESDs of the *P* obtained from the R_1-line shift of the ruby luminescence spectra were estimated to be ±0.05 GPa after averaging repeated measurements.

2.3. Raman spectroscopy

Raman spectroscopy was performed in order to complement FTIR data as the far-infrared region is inaccessible at our FTIR spectrometer imposed by the existing experimental setup (i.e., Globar and mercury-cadmium-telluride detector). Spectra were collected by means of a confocal *Horiba Jobin Yvon LabRAM-HR 800* spectrometer using a red He–Ne laser source emitting light with a wavelength of 632.8 nm and an *Olympus BX41* microscope. An *Olympus LMPIanFL N 50x* objective with a long working distance of 10.6 mm enables to focus the laser beam onto the sample crystal inside the pressure chamber. All in-situ measurements in DACs were carried out using type I anvils in brilliant cuts mounted on Be seats. A diffraction grating with 1800 lines per mm was used for all measurements. High-pressure spectra were acquired using the *LabSpec 6* software (*HORIBA Scientific*) in the spectral range from 100 to 600 cm^{-1} Raman shift with an exposure time of 60 s. The spectral resolution is 0.3 cm^{-1} and the recorded spectra were averaged over 15 individual scans to reduce background noise. Background subtraction and the determination of the band position were achieved using the program *Peakfit v.4* (*Jandel Scientific*). The recorded spectra were fitted with the Gauss-Lorentz-area method. Initial estimates of the number of bands and their distribution in the Raman spectra were based on Chio et al. [39].

2.4. FTIR spectroscopy

High-pressure IR absorption spectra were acquired from a *Bruker*

Hyperion 1000 microscope attached to a *Bruker Tensor 27* FTIR spectrometer in the spectral range from 7000 cm^{-1} to 400 cm^{-1}. The *Hyperion 1000* microscope is equipped with a liquid nitrogen cooled mercury-cadmium-telluride detector and a *Globar* light source. The spectral resolution is 4 cm^{-1} and the spectra were recorded in a time frame of 15 s and averaged over 120 individual scans. The absorption spectra were deconvoluted into single absorption bands with a Voigt-shaped function using the *Peakfit v.4* (*Jandel Scientific*) software. High-pressure spectra were recorded with using type IIa anvils in Boehler-Almax geometry.

2.5. Structure determination

Three individual loadings were carried out for high-pressure intensity data collection with crystal sizes $80 \times 170 \times 40\ \mu m^3$ (loading #1), $85 \times 70 \times 50\ \mu m^3$ (loading #2), $75 \times 175 \times 50\ \mu m^3$ (loading #3). The determination of orientation matrices and all intensity data collections were performed on a *Stoe StadiVari* X-ray diffractometer using a *DECTRIS Pilatus 300K* detector with a 450 µm silicon layer and an air-cooled Incoatec IµS molybdenum micro-focus tube source (50 kV voltage and 1 mA current flow). A total of 3860 frames with angular steps of 0.5° in ω rotational mode with the χ circle fixed to a value ranging from 0° to 90° were collected in 51 runs for each measurement. Data were collected on both sides of the DAC as achieved by a 180° rotation of the ϕ circle after each run. Exposure time was 100 s per frame for the measurement at 9.2 GPa and 60 s for each of the other measurements. Intensities were integrated using the *X-area 1.72* (*STOE & Cie GmbH*) software. Integrated intensities were corrected for absorption due to the sample and DAC components by using the ABSORB code [48]. Indexing of reconstructed reciprocal space yielded monoclinic lattice metrics for the measurements at 2.0, 5.1, and 5.5 GPa, while at 7.3, 8.2 and 9.2 GPa triclinic metrics were found. The structure for the triclinic form was obtained by transforming the positions described in *C*2/*c* setting to the corresponding reduced cell. All refinements were carried out using scattering curves for neutral atoms and isotropic displacement parameters for all atoms using *ShelXle* [49], which is a graphical user interface from the *SHELX* software [50]. Detailed information about the individual instrumental setup and data acquisition can be found in Table 1, the refined positional parameters and displacement parameters are listed in Table 2, and the resulting interatomic distances are given in Table 3.

2.6. High-precision lattice parameters

The lattice parameters were measured on a *Stoe AED II* diffractometer using a Eulerian-cradle geometry and a scintillation counter. The instrument is controlled by the *SINGLE* software [52]. Non-monochromatized Mo radiation (50 kV tube voltage, 30 mA current flow) was used as X-ray source. For each hydrostatic pressure point at least 10 reflections were measured in the 8-position centring mode [53] to refine the unit-cell volume of the quartz reference, which was used as a pressure standard. The corresponding pressure was calculated applying a 4th-order Birch-Murnaghan equation of state [54] using the empirical parameters determined by Scheidl et al. [46]. At least 12 reflections were measured for the sample crystal at each pressure point. Lattice parameters were refined in a first step without any symmetry constraints in order to prove possible deviations in metrics, and were finally constrained to monoclinic symmetry, if appropriate. The resulting metric parameters are listed in Table 4. The equations of state (EoS) were fitted by applying weighted least-square techniques following the Birch-Murnaghan (BM) formalism using the software *EoSFit7* [52]. Normalized pressure-strain analysis were carried out in order to determine the relevant order of truncation of the BM EoS. The obtained EoS parameters are given in Table 5.

Table 1
Crystal data of $FeSO_4 \cdot H_2O$, details of the XRD intensity data collection and data processing, and summary of the structure refinements based on the in-situ high-pressure single-crystal XRD measurements.

P [GPa]	2.0	5.1	5.5	7.3	8.2	9.2
Loading	#1	#3	#2	#1	#3	#1
Space group	*C*2/*c*	*C*2/*c*	*C*2/*c*	*P*1	*P*1	*P*1
a [Å]	7.0445(6)	7.0150(7)	6.9998(5)	5.0048(6)	4.9768(15)	4.9593(11)
b [Å]	7.4366(7)	7.3476(5)	7.3191 (6)	5.0825(13)	5.0898(17)	5.0726(12)
c [Å]	7.6178(7)	7.4661(6)	7.4448(7)	7.3530(29)	7.3316 (16)	7.2889(22)
α [°]	90	90	90	109.462(23)	109.739(19)	109.496(19)
β [°]	118.748(6)	119.086(6)	119.086(6)	109.941(23)	110.025(18)	110.104(23)
γ [°]	90	90	90	92.442(16)	92.245(26)	92.333(19)
V [$Å^3$]	349.89(6)	336.30(5)	333.3(5)	163.18(7)	161.64(8)	159.80(9)
Z	4	4	4	4	4	4
Data collection						
# measured reflections	3748	3534	3710	3645	3135	3492
Rejected	192	154	197	3	72	11
Unique reflections	303	289	292	311	278	293
Max. 2 θ [°]	73.09	73.52	72.22	72.84	73.66	74.04
Range of hkl	−11 =< h =< 7 −8 =< k =< 8 −9 =< l =< 10	−6 =< h =< 8 −7 =< k =< 10 −12 =< l =< 12	−11 =< h =< 11 −9 =< k =< 6 −8 =< l =< 7	−8 =< h =< 8, −5 =< k =< 7 −5 =< l =< 5	−4 =< h =< 6, −6 =< k =< 4, −10 =< l =< 10	−7 =< h =< 7 −5 =< k =< 7 −3 =< l =< 3
R_{Int}	0.0485	0.0310	0.0340	0.0681	0.1230	0.0605
Structure refinement						
r1 ($\|F_O\| > 4\ \sigma$)[a]	0.0441	0.0355	0.0390	0.0477	0.0736	0.0379
wR2[b]	0.118	0.0914	0.0969	0.1149	0.2072	0.0967
GooF[c]	1.122	1.061	1.114	1.076	1.043	1.075
Parameters refined	15	15	15	28	28	28

n = number of reflections, p = number of parameters refined.

[a] $R1 = \sum ||F_O| - |F_c|| / \sum |F_O|$

[b] $wR[w(F_O^2 - F_c^2)^2] / w\left|(F_O^2)\right|\}2\}$

[c] $GooF[w(F_O^2 - F_c^2)^2]/(n-p)\}^{1/2}$.

Table 2
Positional parameters and isotropic displacement parameters of the atom sites in the (a) monoclinic and (b) triclinic $FeSO_4{\cdot}H_2O$ polymorph at 2.0, 5.1, 5.5 and 7.3, 8.2, 9.2 GPa. The atom sites correspond to: (a) Fe at 4*b* $\bar{1}$ (0,½,0), S and Ow at 4*e* **0.2.** (0,y,¼), O1 and O2 at to 8*f* **1** (x,y,z) in *C2/c* (unique axis *b*); (b) FeA at 1*a* $\bar{1}$ (0,0,0), FeB at 1*b* $\bar{1}$ (0,0,½), all other atoms at 2*i* **1** (x,y,z) in $P\bar{1}$.

b				
P [GPa]		7.3	8.2	9.2
FeA	U_{iso}	0.0088(5)	0.0148(9)	0.0094(4)
FeB	U_{iso}	0.0100(5)	0.0149(8)	0.0088(4)
S	x	0.3534(6)	0.3540(14)	0.3522((3)
	y	0.6430(5)	0.6417(15)	0.6401(4)
	z	0.7527(10)	0.7531(3)	0.7532(8)
	U_{iso}	0.0080(5)	0.0121(9)	0.0070(4)
O1A	x	0.6306(17)	0.6453(40)	0.6297(11)
	y	0.7135(16)	0.7226(42)	0.7175(13)
	z	0.9237(28)	0.9288(11)	0.9361(23)
	U_{iso}	0.0155(14)	0.0222(20)	0.01311(12)
O2A	x	0.1156(15)	0.1139(42)	0.1072(10)
	y	0.6550(14)	0.6484(44)	0.6500(11)
	z	0.8325(25)	0.8282(11)	0.8283(23)
	U_{iso}	0.0081(13)	0.0188(19)	0.0115(12)
O1B	x	0.682(16)	0.6901(39)	0.6792(10)
	y	0.6427(14)	0.6509(40)	0.6476(11)
	z	0.4006(26)	0.4010(11)	0.3971(22)
	U_{iso}	0.0090(13)	0.0226(21)	0.0108(11)
O2B	x	0.3380(16)	0.3436(40)	0.3367(10)
	y	0.8535(15)	0.8520(42)	0.8422(12)
	z	0.6522(25)	0.6565(10)	0.6503(23)
	U_{iso}	0.0120(14)	0.023(21)	0.0114(12)
Ow	x	0.8471(15)	0.8430(38)	0.8475(10)
	y	0.1502(15)	0.1511(42)	0.1500(12)
	z	0.7478(26)	0.7497(9)	0.7510(2)
	U_{iso}	0.0100(13)	0.0148(18)	0.0101(11)
a				
P [GPa]		2.0	5.1	5.5
Fe	U_{iso}	0.0098(4)	0.0086(3)	0.0083(3)
S	y	0.1498(3)	0.1460(2)	0.1455(2)
	U_{iso}	0.0081(5)	0.0072(4)	0.0062(3)
O1	x	0.1689(6)	0.1681(7)	0.1684(5)
	y	0.0369(7)	0.0329(5)	0.0323(5)
	z	0.4034(7)	0.4090(5)	0.4115(7)
	U_{iso}	0.0148(8)	0.0144(7)	0.0121(7)
O2	x	0.0984(6)	0.1033(7)	0.1037(5)
	y	0.2657(6)	0.2646(4)	0.2637(5)
	z	0.1581(7)	0.1609(5)	0.1610(6)
	U_{iso}	0.0128(9)	0.0119(7)	0.0109(7)
Ow	y	0.6480(9)	0.6500(6)	0.6500(7)
	U_{iso}	0.0132(11)	0.0102(8)	0.0110(9)

3. Results

3.1. High-pressure vibrational spectroscopy

Raman spectra under hydrostatic pressure conditions using Ar as the pressure-transmitting medium were recorded in a sequence of 13 pressure points between 10^{-4} and 9.19 GPa in pressure steps between 0.33 and 1.57 GPa. A focus on the internal modes in the wavenumber range between 100 and 600 cm^{-1} shift (Fig. 2a) revealed the most prominent bands as described by Chio et al. [39], i.e. the lattice modes at 116, 218, 272, 423, and 495 cm^{-1} (at ambient pressure). The four strongest peaks could be assigned following Chio et al. [39] to either translational modes (218 and 272 cm^{-1}) related to the one octahedrally coordinated Fe position and the H_2O ligand, and to the $\tilde{\nu}_2$ mode of the SO_4 group (423 and 495 cm^{-1}). The high-pressure spectra reveal the typical redshift with $\Delta\tilde{\nu}/\Delta P$ values between 1.29(5) and 8.3(3) $cm^{-1}GPa^{-1}$ (Fig. 2b). None of the recorded modes reveals, apart from the positional shift, any evidence for changes such as splitting or an emerging shoulder, which would be indicative for additional independent crystallographic sites as originating from lowering the symmetry, the occurrence of a superstructure or the modulation of the lattice.

Nevertheless, in the low-frequency regime, i.e. below 350 cm^{-1} shift, the spectra at pressures $\geq$ ~6.15 GPa show at least three weak new modes located at 128, 189 and 332 cm^{-1} (as determined in the spectrum at 9.19 GPa). These faint spectral features are the only trackable changes within the experimental range of investigations. The rather unexciting spectral changes suggest that both the topological arrangement and the short-range order remain more or less unchanged under steadily increasing hydrostatic loads up to the hydrostatic limit at around 9–10 GPa.

The series of in total 10 infrared spectra recorded between 10^{-4} and 8.54 GPa provide at a first glance a similar view. The spectra (Fig. 3) are characterized by the $\tilde{\nu}_1$ and $\tilde{\nu}_3$ modes of the SO_4 tetrahedra within the 1000-1200 cm^{-1} range, and the $\tilde{\nu}_1$, $\tilde{\nu}_2$ and $\tilde{\nu}_3$ modes of the H_2O molecules at 1400-1800 cm^{-1} and 3200-3500 cm^{-1}. The main spectral features remain apparently unchanged. At a closer look the band position of the $\tilde{\nu}_1$ mode as obtained from spectral deconvolution of the 3200-3500 cm^{-1} absorption feature into four individual absorption bands, it is obvious that the linear trend of positional shift changes again at pressures beyond ~6.0 GPa (Fig. 4). Together with the findings from Raman spectroscopy, it confirms subtle changes at a critical pressure lying between 5.9 and 6.5 GPa. These changes obviously are related to changes of interatomic distances between donor and acceptor oxygen atoms within the hydrogen bonding system.

3.2. Structural crystallography at high-pressures

Three individual loadings with 4:1 methanol-ethanol fluid as a pressure transmitting medium and *Boehler-Almax* type diamonds were carried out to collect diffraction images at six pressures (i.e. 2.0, 5.1, 5.5, 7.3, 8.2 and 9.2 GPa). Sample single crystals were $80 \times 170 \times 40\ \mu m^3$ (loading #1), $85 \times 70 \times 50\ \mu m^3$ (loading #2), $75 \times 175 \times 50\ \mu m^3$ (loading #3) in size. Data processing of the recorded intensities at pressures $\leq$5.50 GPa clearly verified the lattice settings in the reported *C2/c* space-group symmetry and any unconstrained refinement of base vectors confirmed the monoclinic metrics within the 1σ criterion of the obtained uncertainties. This is in contrast to the lattice metrics observed for the data sets $\geq$7.30 GPa, which clearly suggest triclinic lattice symmetry. The inspection of the reconstructed reciprocal lattice moreover suggests symmetry breaking due to the violation of serial and zonal extinction as typical for *c*- and *n*-glide planes and 2_1-screw axis in $P\bar{1}$. Hence, the setting for the triclinic primitive unit-cell corresponds to the reduced cell in the monoclinic *C*-lattice as depicted in Fig. 5, with a simple relationship between the unit-cell volumes as of $V_{triclinic} = ½\ V_{monoclinic}$. The reconstructed reciprocal space has also been scanned for the occurrence of any superstructure reflections, satellite reflections, and diffuse scattering, which all can ultimately be ruled out to occur in any of the collected intensity data sets.

Final refinements of the crystal structures were carried out based on models with atomic positions provided by Bechtold and Wildner [30] for *C2/c* setting. Since the hydrogen atom positions were not determined in any of the herein reported high-pressure crystal structures the O3 oxygen [25,27,30] was named O_w instead in order to unambiguously denote the donor oxygen of the hydrogen bond. The structural model reported by Giester [35] for $CuSO_4{\cdot}H_2O$ in $P\bar{1}$ served as basis for the structure determination of the high-pressure polymorph, but was transformed to a cell setting where $c_{triclinic} = c_{monoclinic}$ according to the transformation matrix (−1/0/0//0/-1/0//1/1/1) to allow a better comparison of the low-pressure and high-pressure polymorphs. The *C2/c* - $P\bar{1}$ transition results in a splitting of structural sites, i.e. FeA and FeB and twice as many

Table 3
Selected interatomic distances (Å) and bond angles (°) in $FeSO_4{\cdot}H_2O$ calculated from the positional parameters as given in Table 2.The Δ_{oct} parameter describes the octahedral distortion as defined by Brown and Shannon [51]. Note that for *C2/c* symmetry (i.e. for $P \leq 5.5$ GPa) the atoms labeled A and B are identical and do not require differentiation.

P (GPa)	10^{-4}	2.0	5.1	5.5	7.3	8.2	9.2
interatomic distances (Å)							
FeA-O1A (2x)	2.103(1)	2.099(4)	2.099(4)	2.095(3)	2.091(7)	2.015(26)	2.097(9)
FeA-O2A (2x)	2.050(1)	2.041(5)	2.028(3)	2.027(4)	2.015(5)	2.039(8)	2.013(7)
FeA-Ow (2x)	2.228(1)	2.200(3)	2.168(2)	2.161(3)	2.152(20)	2.142(13)	2.114(16)
$<FeA^{[6]}\text{-}O>$	2.127	2.113	2.098	2.094	2.086	2.065	2.075
$\Delta_{oct}(FeAO_6)$	1.23	0.97	0.74	0.68	0.94	0.71	0.45
FeB–O1B (2x)	= FeA-O1A	= FeA-O1A	= FeA-O1A	= FeA-O1A	2.095(7)	2.052(25)	2.084(7)
FeB–O2B (2x)	= FeA-O2A	= FeA-O2A	= FeA-O2A	= FeA-O2A	2.010(14)	2.037(6)	2.016(9)
FeB-Ow (2x)	= FeA-Ow	= FeA-Ow	= FeA-Ow	= FeA-Ow	2.136(13)	2.152(11)	2.137(14)
$<FeB^{[6]}\text{-}O>$	$=<FeA^{[6]}\text{-}O>$	$=<FeA^{[6]}\text{-}O>$	$=<FeA^{[6]}\text{-}O>$	$=<FeA^{[6]}\text{-}O>$	2.080	2.080	2.079
$\Delta_{oct}(FeBO_6)$	$=\Delta_{oct}(FeAO_6)$	$=\Delta_{oct}(FeAO_6)$	$=\Delta_{oct}(FeAO_6)$	$=\Delta_{oct}(FeAO_6)$	0.45	0.61	0.59
S–O1A	1.462(1)	1.466(5)	1.459(4)	1.464(4)	1.450(15)	1.499(14)	1.473(10)
S–O1B	= S–O1A	= S–O1A	= S–O1A	= S–O1A	1.466(6)	1.487(15)	1.467(6)
S–O2A	1.491(1)	1.477(4)	1.482(3)	1.477(4)	1.491(10)	1.474(24)	1.491(13)
S–O2B	= S–O2A	= S–O2A	= S–O2A	= S–O2A	1.480(19)	1.463(23)	1.449(17)
<S–O>	1.477	1.472	1.471	1.471	1.472	1.489	1.470
Ow···O1A	3.240(3)	3.134(7)	3.058(5)	3.047(6)	3.130(13)	3.114(27)	3.152(10)
Ow···O1B	= Ow···O1A	= Ow···O1A	= Ow···O1A	= Ow···O1A	2.906(12)	2.868(27)	2.839(8)
Ow···O2A	2.756(2)	2.712(4)	2.664(5)	2.653(4)	2.618(12)	2.602(28)	2.587(10)
Ow···O2B	= Ow···O2A	= Ow···O2A	= Ow···O2A	= Ow···O2A	2.646(13)	2.606(27)	2.651(9)
bond angles (°)							
FeA-Ow-FeB	121.42(7)	119.985(2)	118.878(2)	118.930(2)	118.04(71)	117.27(30)	118.02(49)
FeA-O1A-S	136.75(11)	133.92(31)	131.25(25)	130.44(26)	131.20(75)	131.05(72)	126.60(50)
FeA-O2A-S	133.57(9)	132.41(32)	130.97(19)	130.70(23)	128.22(60)	126.49(75)	126.56(48)
FeB–O1B–S	= FeA-O1A-S	= FeA-O1A-S	= FeA-O1A-S	= FeA-O1A-S	129.784(72)	131.72(72)	128.80(51)
FeB–O2B–S	= FeA-O2A-S	= FeA-O2A-S	= FeA-O2A-S	= FeA-O2A-S	131.30(75)	130.51(70)	132.05(54)
O1A-Ow-O1B	80.00(5)	78.46(12)	77.08(12)	76.99(12)	78.92(49)	80.20(43)	80.41(35)
O2A-Ow-O2B	46.19(4)	45.85(12)	45.88(8)	45.90(10)	46.17(31)	45.52(55)	45.85(23)
O1A-Ow-O2B	67.31(4)	66.36(12)	65.06(10)	64.89(11)	63.86(45)	63.05(48)	63.01(29)
O1B-Ow-O2A	= O1A-Ow-O2B	= O1A-Ow-O2B	= O1A-Ow-O2B	= O1A-Ow-O2B	64.86(42)	64.38(47)	64.87(32)

independent oxygen sites (O1A, O1B, O2A, O2B). An overview of the in total 6 refined high-pressure structures is given in Table 2. R_{int} values vary from 0.031 to 0.123 providing evidence for the correct Laue symmetry and a sufficient data quality on merging symmetry equivalents. $R1_{obs}$ values lie within the range 0.036 and 0.076, the goodness of fit ranges from 1.043 to 1.122. Due to the low symmetry and having only one single-crystal orientation within the DAC, all refinements were carried out with only isotropic displacement parameters.

The variation of interatomic distances with pressure (Table 3) reveals no significant changes for the Fe–O and S–O bond distances, even across the supposed critical point related to the observable symmetry change. The FeO_6 octahedra (a unique one in *C2/c*, two independent in $P\bar{1}$) show an unspectacular quasi linear decrease of their values with pressure. It is noteworthy that the longer Fe-Ow distances are subject to greater compressibility, and thus the polyhedral distortion decreases with pressure and the FeO_6 octahedra become slightly more regular. The values for Δ_{oct} (ranging from 0.97 to 0.45) are for any of the structures reported here significantly smaller than the polyhedral distortion of the equivalent sites in $CuSO_4{\cdot}H_2O$ ($\Delta_{oct} = 11.11$ and 8.16) [35]. A comparable picture of the stereochemical changes can be found for the SO_4 tetrahedral units, with continuous marginal decrease in S–O bond distances.

While the individual FeO_6 and especially SO_4 building units appear to be rather rigid and do not provide any evidence of a significant change associated with the supposed structural transformation, the disappearance of individual symmetry elements enables new freedom of tiltings for the interpolyhedral connections within the given framework topology. The changes of bond angles at bridging oxygen atoms undergo small changes, with a general trend towards slightly smaller angles (cf. Table 3). The Fe-Ow-Fe angle, which is the angle within the corner sharing $[FeO_4(H_2O)]^{6-}$ octahedral chains across the bridging Ow atom, is reduced from ~121.4° to ~118.0° due to the subtle tilting of the cross-linking SO_4 units as getting rid of their former twofold axis. The Fe–O–S angles, which are measuring between ~136.8° and ~133.6°, get simultaneously reduced to values ranging between ~126.6° and ~132.1°. They reflect the trend to compact the FeO_6–SO_4-framework by folding on the bridging oxygen atoms.

As a significant consequence of the tilting and associated rotation of the SO_4 groups, the O···O contacts that are available for the hydrogen-bonding system are also being changed (Fig. 6). While the symmetry-equivalent distances between the short Ow···O1 and the long Ow···O2 distances were the same due to the symmetry constraints in *C2/c*, the change to a triclinic lattice metrics leads to a significant diversification of the previously equal distances, with unmistakable differences for O1A versus O1B and O2A versus O2B (Fig. 7). As expected, the long (Ow···O1) and the short (Ow···O2) distances behave differently. A very clear diversification can be observed for the weak Ow···O1 contacts (measuring 3.24 Å at 1 bar), which get reduced to $2 \times \sim 3.05$ Å as determined at 5.5 GPa just before the phase transition occurs. Beyond the critical pressure of the phase transformation, the distance to O1A increases again significantly while the distance to O1B is reduced to 2.91 Å. An approximately comparable disproportionation into one longer and one shorter distance – although to a lower extent – can also be observed for the short Ow···O2 contacts with slightly longer distances to O2B and shorter to O2A (see Fig. 7). The observed changes of the relevant distances in the hydrogen-bonding system suggest the formation of a bifurcated Ow-H::O1B/O2B hydrogen bridge on one side, in return O2A being the unique acceptor for the other Ow-H···O2B bridge involving the second hydrogen atom of the H_2O molecule.

3.3. Compressibility and elastic properties

Precise unit-cell parameters were determined from XRD Bragg peaks under hydrostatic conditions within the pressure range 10^{-4} to 8.4 GPa (Table 4). For comparability between monoclinic and triclinic lattices, the metric parameters for the monoclinic *C2/c* polymorph are provided in the setting of the reduced cell, which corresponds to the base vectors of the triclinic setting (cf. Fig. 5). The analysis of the 15 individual data points, as derived from subsequent compression of a single crystal and

Table 4
Unit-cell parameters of the symmetry unconstrained reduced cell (a, b, c, α, β, γ, V) and the symmetry-constrained values a_m, b_m and β_m for $FeSO_4{\cdot}H_2O$ as derived from least-squares refinement of the monoclinic $C2/c$ cell. Note that the value for c_m is equivalent to c in the reduced cell; the volume $V_m = 2 \times V_{red}$ (The suffix "m" and "red" denote the setting of the monoclinic $C2/c$ cell and the reduced cell which coincides with the triclinic $P\bar{1}$ cell respectively).

V_{Qtz} [Å^3]	P [GPa]	a_{red} [Å]	b_{red} [Å]	$c_{red} = c_m$ [Å]	α_{red} [°]	β_{red} [°]	γ_{red} [°]	V_{FSH} [Å^3]	a_m [Å]	b_m [Å]	α_m [°]	β_m [°]	γ_m [°]
112.968(3)	0.00010(1)	5.1772(2)	5.1770(2)	7.7786(5)	109.140(4)	109.130(4)	93.673(3)	182.613(15)	7.0823(2)	7.5525(2)	90	118.631(3)	90
110.058(27)	1.052(11)	5.1502(3)	5.1489(4)	7.6973(6)	109.258(7)	109.253(5)	93.320(7)	178.706(20)	7.0689(3)	7.4906(5)	90	118.731(3)	90
107.535(10)	2.137(5)	5.1266(5)	5.1257(2)	7.6250(4)	109.375(4)	109.379(6)	93.045(5)	175.283(19)	7.0538(4)	7.4389(5)	90	118.827(2)	90
106.853(18)	2.460(9)	5.1183(3)	5.1200(4)	7.6030(5)	109.401(6)	109.389(5)	93.000(6)	174.278(20)	7.0474(3)	7.4269(6)	90	118.848(2)	90
104.938(11)	3.441(6)	5.1001(6)	5.1003(3)	7.5481(5)	109.496(5)	109.477(7)	92.804(8)	171.637(22)	7.0341(4)	7.3877(7)	90	118.934(3)	90
103.397(16)	4.314(10)	5.0860(6)	5.0854(4)	7.5043(11)	109.563(7)	109.554(9)	92.697(8)	169.553(31)	7.0212(3)	7.3594(6)	90	119.017(3)	90
102.393(16)	4.925(10)	5.0757(9)	5.0764(2)	7.4730(7)	109.614(5)	109.608(10)	92.609(8)	168.116(33)	7.0137(6)	7.3407(7)	90	119.070(4)	90
101.702(6)	5.366(5)	5.0696(3)	5.0707(4)	7.4505(6)	109.618(6)	109.646(5)	92.583(6)	167.189(20)	7.0070(3)	7.3292(5)	90	119.105(3)	90
100.824(7)	5.951(5)	5.0623(4)	5.0608(4)	7.4244(6)	109.679(7)	109.667(6)	92.520(7)	165.974(22)	6.9993(2)	7.3137(5)	90	119.150(3)	90
100.529(6)	6.154(3)	5.0573(3)	5.0593(5)	7.4161(7)	109.684(7)	109.707(6)	92.491(6)	165.538(22)	6.9963(5)	7.3073(6)	90.010(7)	119.165(5)	90.023(7)
100.307(6)	6.309(4)	5.0419(4)	5.0700(5)	7.4079(7)	109.794(8)	109.596(7)	92.476(8)	165.207(23)	6.9940(7)	7.3030(7)	90.054(7)	119.159(7)	90.319(8)
99.685(14)	6.753(10)	5.0213(7)	5.0778(5)	7.3867(7)	109.573(7)	109.957(9)	92.385(11)	164.193(31)	6.9910(8)	7.2883(11)	90.100(10)	119.240(7)	90.642(11)
98.942(6)	7.303(4)	5.0033(3)	5.0825(6)	7.3615(9)	109.515(8)	110.029(6)	92.406(6)	163.168(26)	6.9807(6)	7.2801(6)	90.124(8)	119.255(6)	90.900(7)
98.457(13)	7.699(5)	4.9915(3)	5.0833(5)	7.3440(7)	109.508(6)	110.083(6)	92.377(7)	162.377(22)	6.9749(6)	7.2704(6)	90.130(7)	119.282(6)	91.045(7)
97.543(9)	8.398(8)	4.9719(3)	5.0838(5)	7.3138(7)	109.505(7)	110.148(6)	92.339(7)	161.037(23)	6.9644(6)	7.2545(6)	90.119(7)	119.316(6)	91.276(7)

Table 5
Least-square fitted 3rd order Birch-Murnaghan equations of state parameters of the unit-cell volume and lattice vectors for the $FeSO_4{\cdot}H_2O$ polymorphs.

P-range (GPa)	X_0	K_0, M_0 (GPa)	K', M'	χ^2
0.0001–5.94	$V_0 = 365.23(30)$	$K_0 = 45.2(2)$	$K' = 6.7(1)$	0.53
	$a_m = 7.0823(2)$	$M_0 = 496(9)$	$M' = 1.3(3.2)$	4.0
	$b_m = 7.5525(2)$	$M_0 = 109(2)$	$M' = 36(2)$	1.92
	$c_m = 7.7786(5)$	$M_0 = 93.8(7)$	$M' = 13.1(4)$	3.54
6.15–8.4	$V_0 = 367.0(4)$	$K_0 = 45.11(57)$	$K' = 5.4$	0.93
	$a_m = 7.087(4)$	$M_0 = 471(19)$	$M' = 3.0$	3.66
	$b_m = 7.54(1)$	$M_0 = 112(7)$	$M' = 36.8$	3.89
	$c_m = 7.784(4)$	$M_0 = 102(1)$	$M' = 9.1$	0.3

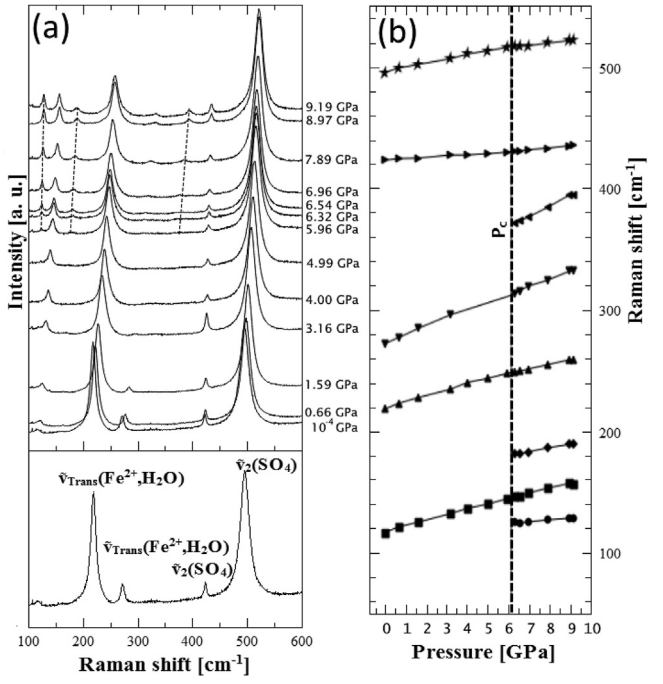

Fig. 2. (a) Series of high-pressure Raman spectra of $FeSO_4{\cdot}H_2O$ pressurized hydrostatically in the range 1 bar–9.19 GPa using argon as pressure-transmitting medium. Within the presented wavenumber range the spectra ≤5.96 GPa reveal five of the known lattice modes reported by Chio at al [39]. Between 5.96 GPa and 6.32 GPa three additional weak modes (at 128, 189 and 332 cm^{-1} as determined in the spectrum at 9.19 GPa, see dashed lines) are indicative for a subtle phase transition between 5.96 and 6.32 GPa. (b) Plot of the Raman shift of vibrational modes in the spectral region from ~100 to ~550 cm^{-1} Raman shift as a function of pressure.

using a reference quartz crystal for precise pressure calibration, show an apparently consistent compression behaviour in terms of the volume evolution (Fig. 8a). The volume data do not give evidence, at a first glance, for a discontinuity at ~6 GPa as manifested by the changes reported above. Nevertheless, on fitting the P–V data points with a conventional third-order Birch-Murnaghan equation of state (BM-3 EoS), the values for the unit-cell volumes (Table 5) beyond ~6 GPa fall slightly below the extrapolated line (red line in Fig. 8a) with increasing deviations in a quasi linear fashion as indicated by the differences plotted in blue. The compression moduli are described by the bulk modulus $K_0 = 45.2 \pm 0.2$ GPa and its dimensionless pressure derivative $K' = 6.75 \pm 0.13$. Normalized pressure strain analysis revealed a strong discontinuity for each of the lattice parameters as well as the unit-cell volume after the critical pressure of transformation. K' and M' for the high-pressure polymorph (HPP) were fixed to values estimated from this data since refinement of these parameters did not provide meaningful fits due to a relatively variable V_0 and M_0 of the unquenchable high-pressure

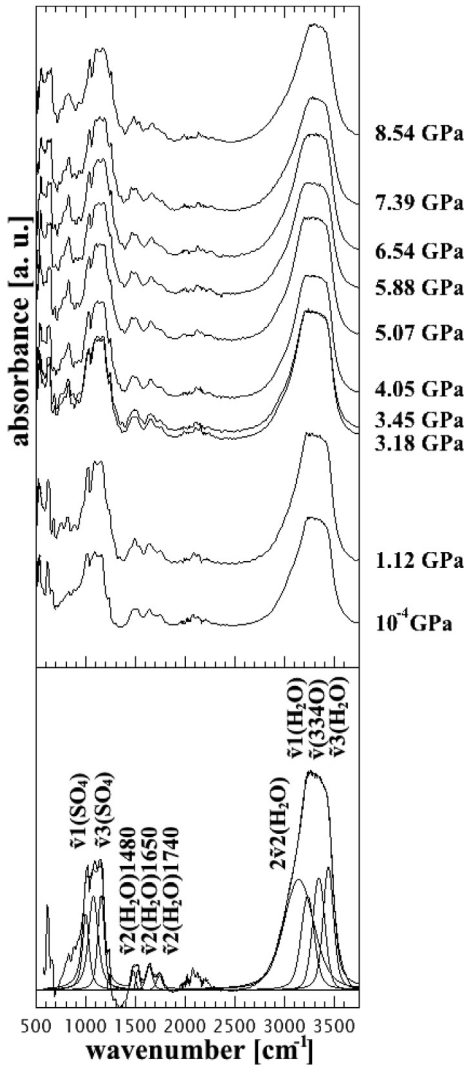

Fig. 3. Series of infrared spectra of $FeSO_4{\cdot}H_2O$ hydrostatically compressed in Ar in the range 10^{-4} to 8.54 GPa. The band assignment of bands follows [39].

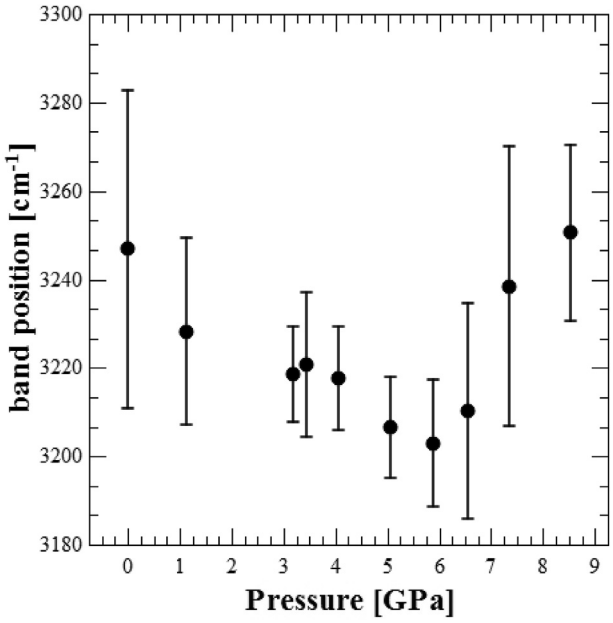

Fig. 4. The evolution of the band positions of the $\tilde{\nu}_1$(OH) band in IR spectra of $FeSO_4{\cdot}H_2O$, corresponding to the values obtained after peak fitting using unconstrained Voigt-shaped functions for spectral deconvolution with four band components. Vertical error bars indicate the individual positional uncertainties. The errors for P (≈0.05 GPa) are smaller than the symbol size. The plot indicates a distinct discontinuity across a critical pressure between 5.88 and 6.54 GPa.

phase. It should be noted that fixing K' to a value without a given estimated standard deviation results in underestimation of the standard deviation for the free parameters V_0 and K_0. Using the 7 data points at ≥ 5.95 GPa, the refinements of EoS parameters with K' being constrained to 5.4 yields $K_0 = 45.1 \pm 0.6$ GPa and $V_0 = 367.0 \pm 0.4$ thus revealing that K_0 remains apparently unchanged, while K' gets significantly reduced. This is further supported by the evolution of normalized pressure as a function of Eulerian finite strain, clearly demonstrating a change in the compression mechanism after the critical pressure of transformation for the volume data accounting for significant deviations dK/dP of the HPP relative to the low-pressure polymorph (Fig. 9a). Similar behaviour was observed for the c-lattice parameter (Figs. 8f *and* 9b*)*. While the volume (Fig. 8a) and c-axis (Fig. 8d*)* evolution provide only subtle indication of a phase transformation, the variations of the a_{red} and b_{red} lattice parameters of the reduced unit-cell, which lie in the a-b-plane of the monoclinic cell-setting, clearly show the changes related to the lattice metrics (Fig. 8b–e).

Axial compressibility of the monoclinic lattice vectors a_m, b_m and c_m reveal strong compressional anisotropy with 29% higher compressibility of the [001] direction relative to the [100] direction. The variation of the monoclinic lattice parameters with pressure is almost continuous as reflected by merely subtle changes of the EoS parameters as determined for both the LPP and the HPP. The orientation and magnitude of the principal axis of the strain ellipsoid were calculated using the Win_Strain software [55]. The strain ellipsoid is constrained due to monoclinic symmetry of the LPP with the eigenvalue e_2 (= -0.03211 ± 0.00008) being//[010], and e_1 and e_3 lying within the (010) plane. The angle between the crystallographic c-axis and e_1 (= -0.05206 ± 0.00009) and e_3 (= -0.01104 ± 0.00005) principal strain axis directions is around 20° and 110°, respectively. The principal strain axis reveal a pronounced anisotropic elastic behaviour with relative values e_1: e_2: $e_3 = 4.7 : 2.9 : 1$ as determined from lattice changes between 1 bar and 5.9 GPa, thus confirming the direction close to the c-axis to be the most compressible and the direction approximating the a-axis to be the stiffest lattice direction. In the HPP symmetry breaking shear strain components e_{12} and e_{21} arise. The monoclinic to triclinic phase transition is dominated by the e_{12} component, which is attributed to large deviations of the angle γ from 90° beyond P_c. e_{23} is about one order of magnitude smaller than e_{12}, which is in excellent agreement which subtle deviations from 90° for the α_m compared to rather large deviations for γ_m (Fig. 10a). A positive e_3 eigenvalue (= 0.00275 ± 0.00015) with $a_m \angle$ 128.1 $b_m \angle$ 46.3 $c_m \angle$ 81.2 as determined between 6.15 and 6.3 GPa reflects the discontinuous behaviour of the b_{red} (=$[\bar{1}10]_m$) axis displaying negative compressibility beyond P_c (Fig. 8c). Contrary to this behaviour the e_1 (-0.00367 ± 0.00016 with $a_m \angle$ 59.1 $b_m \angle$ 44.1 $c_m \angle$ 81.2) component is the direction of maximum compressibility as reflected in the strong decrease of the a_{red} (=$[110]_m$) axis (Fig. 8b*)*.

Compared to highly hydrated sulfate minerals (i.e., $MgSO_4{\cdot}11H_2O$: $K_0 = 19.9(4)$, $K' = 9(1)$ [4]; $MgSO_4{\cdot}9H_2O$: $K_0 = 19.5(3)$, $K' = 3.8(4)$ [3], $MgSO_4{\cdot}7H_2O$: $K_0 = 21.5(1)$, $K' = 5.4$ [18,56], β-$MgSO_4{\cdot}5H_2O$: $K_0 = 31.4(4)$, $K' = 5.4(1)$ [19], $NaSO_4{\cdot}10H_2O$: $K_0 = 19.6(1)$, $K' = 5.8(5)$ [57]) $FeSO_4{\cdot}H_2O$ reveals a remarkable stiffness, which is attributed to the rigid tetrahedral-octahedral framework of the kieserite structure type in contrast to topologies consisting of isolated polyhedra or dimers (e.g. in β-$MgSO_4{\cdot}5H_2O$) linked by intramolecular hydrogen bonds. Low hydrated sulfate minerals with a higher degree of polyhedral polymerization (i.e., bloedite ($Na_2Mg(SO_4)_2{\cdot}4H_2O$): $K_0 = 39.9(6)$ GPa, $K' = 4$ [58,59], kainite ($KMgSO_4Cl{\cdot}3H_2O$), $K_0 = 32.2(5)$, $K' = 3.8(1)$ [60], gypsum ($CaSO_4{\cdot}2H_2O$): $K_0 = 44(3)$ GPa, $K' = 3.3(3)$) are better suited for a comparison of the structural evolution under high-pressure conditions.

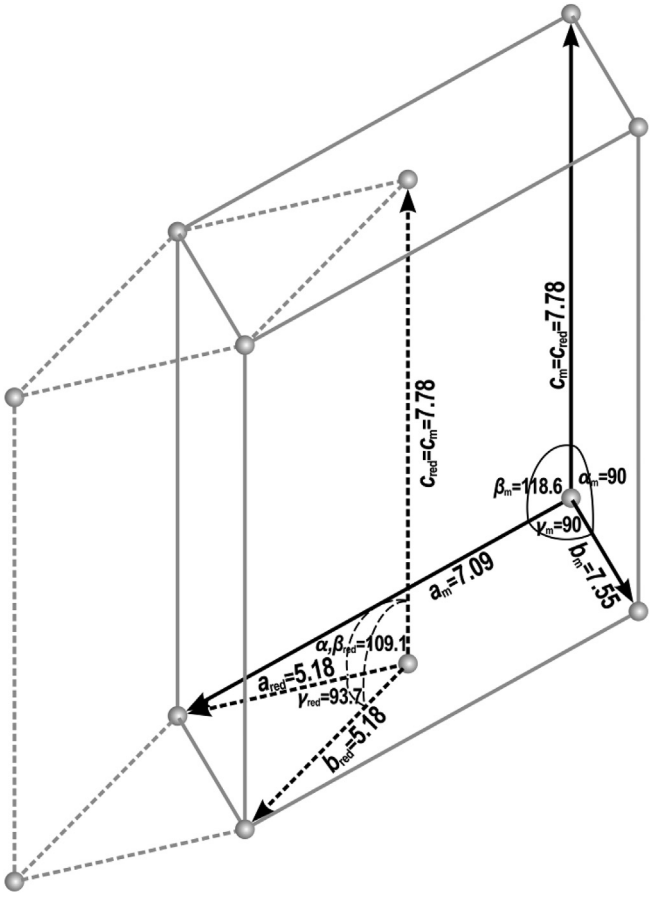

Fig. 5. Relationship between the monoclinic *C*-centred unit cell (solid lines; $a_m = 7.09$ Å, $b_m = 7.55$ Å, $c_m = 7.78$ Å, $\beta_m = 118.6°$) and the reduced cell (dashed lines), whose base vectors correspond to the setting of the triclinic *P* lattice ($a_{red} = b_{red} = 5.18$ Å, $c_{red} = 7.78$ Å, $\alpha_{red} = \beta_{red} = 109.1°$, $\gamma_{red} = 93.7°$) for $FeSO_4 \cdot H_2O$ at ambient conditions (*Talla and Wildner*, in prep). Note that the direction of the *c*-axis is equivalent in both settings.

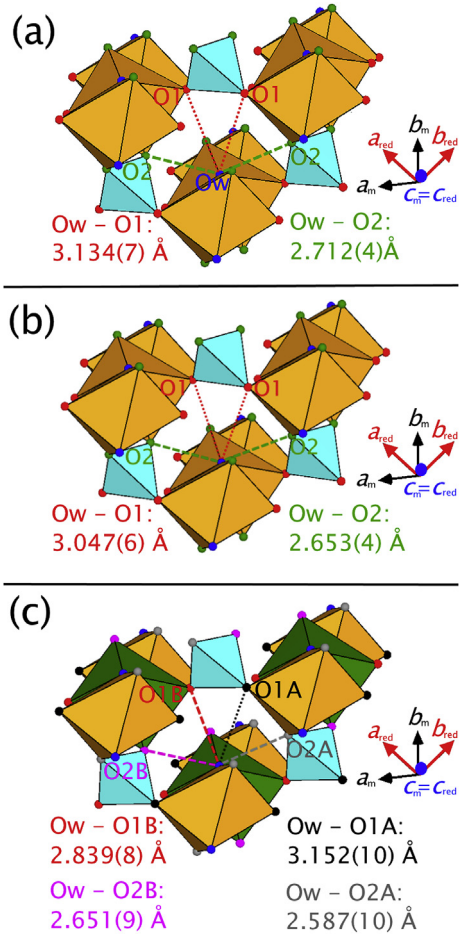

Fig. 6. Comparison of the hydrogen-bonding scheme in $FeSO_4 \cdot H_2O$ at (a) 2.05, (b) 5.50, and (c) 9.2 GPa. While the each two Ow-H···O1 and Ow-H···O2 distances are equivalent in the *C*2/*c* low-*P* polymorph as determined by the point symmetry of the Ow sites (Fig. 6a + *b*.), the equivalent donor-acceptor distances in the high-pressure structure take different values (Fig. 6c.). Hydrogen bonds with Ow-H···O > 3 Å are represented by puncted lines, shorter ones by dashed lines.

Both bloedite and kainite did not reveal any evidence for a structural phase transition up to 11.2 and 14 GPa, respectively, whereas gypsum transforms at ~4 GPa [61,62]. Gypsum, shows the maximum compressibility perpendicular to the water molecule interlayer, i.e. along [010] direction. The bloedite structure is built up from rigid $[Mg(H_2O)_4SO_4)_2]^{2-}$ units, which are connected through soft Na–O bonds and hydrogen bridges. In kainite the presence of relatively stiff magnesia octahedra in the interlayer prevents this direction to be the most compressible. In contrast to this sheet like structures, $FeSO_4 \cdot H_2O$ forms a three-dimensional framework, thus a comparison with the above mentioned compounds is only possible to a limited extent. All these compounds have in common that the compression behaviour seems to be mainly controlled by the linkage and degree of polymerization of rigid divalent cation polyhedra and sulfate tetrahedra and relatively soft intramolecular hydrogen bonds thus accounting for the increasing stiffness of hydrated sulfate minerals as hydration stage decreases and the degree of polymerization increases.

3.4. Nature of phase transition

At a certain point at about 6 GPa, the lattice angles indicate a deviation from the monoclinic symmetry, corresponding to an increasingly pronounced triclinic distortion. This is manifested through the evolution of the two angles α_{red} and β_{red} (Fig. 10b), which are equivalent within their uncertainties up to the critical pressure, whereas one value significantly increases while the other significantly decreases above P_c. This can also be demonstrated for the angles in the monoclinic setting, where both α_m and γ_m (which are 90° within their uncertainty) reveal values being significantly different from 90° as it would be required for a monoclinic setting (Fig. 10a). These changes in the lattice metrics clearly indicate, that at the critical transition point the crystal structure undergoes a monoclinic-to-triclinic transition from geometrical point of view, which in turn supports the findings from reflection conditions suggesting a *C*2/*c*-to-$P\bar{1}$ transformation. The phase transition can be classified as being proper ferroelastic, featuring analogies to various similar transitions such as the reversible transition from rutile-type GeO_2 to the $CaCl_2$-structure [63] and isostructural compounds (e.g. SiO_2: [64–67]). Similar appearance of a reversible transition has been reported for the scheelite-to-fergusonite transformation in orthotungstates and orthomolybdates, being a second-order ferroelastic one as manifested by the arising spontaneous strain [68,69].

An order-parameter analysis was carried out in order to classify the structural phase transition as identified within the scope of the measurement of precise lattice parameter. The variation of both the *a* and the *b* lattice parameter with pressure were chosen as order parameters. The experimentally determined values for K_0 and K' of the monoclinic low-pressure polymorph (LPP) were used to calculate the corresponding lattice parameter as determined through the BM EoS for the pressure points higher than the critical pressure of transformation. The differences between the observed and calculated values Δ_{o-c} where determined through

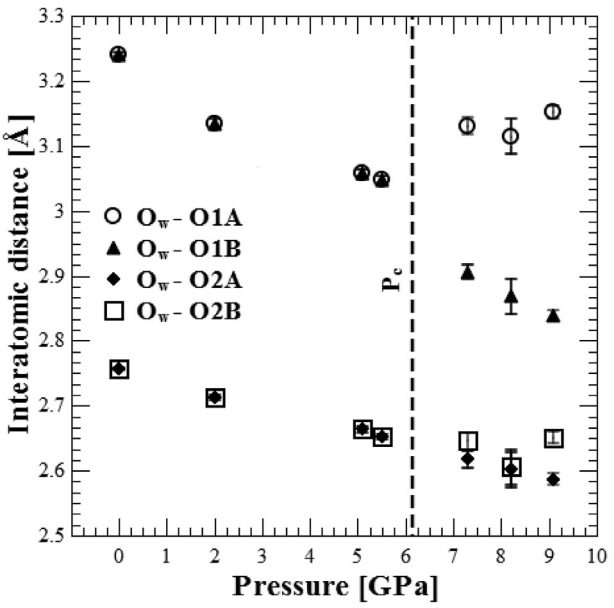

Fig. 7. Evolution of the various Ow···O1 and Ow···O2 donor-acceptor distances with pressure as relevant for the hydrogen-bonding system in the two polymorphs of $FeSO_4{\cdot}H_2O$.

a_{obs}-a_{calc} and b_{obs}-b_{calc} for the respective lattice direction and plotted as shown in Fig. 11. As the $\Delta_{o\text{-}c}$ (= a_{obs}-a_{calc} or b_{obs}-b_{calc}) follows the power law $\Delta_{o\text{-}c} \propto |P\text{-}P_c|^{\beta}$ with β being the critical exponent, fitting to the data points beyond $P \approx 6.1$ GPa yields the parameters for the critical transition pressure P_c and the critical exponent β, the latter one being very characteristic for the nature of the transition (i.e. if the character of the structural phase transition is first order, second order or a tricritical one). Both data sets (Fig. 11) yield independently a value for P_c of 6.154 ± 0.001 GPa with β being 0.52 ± 0.01 and 0.53 ± 0.01, respectively. The value for the critical exponent being ~0.50 confirms the nature of the transition to be second-order in character, as also suggested by the apparent lack of a distinct volume discontinuity. Calculating the values of the unit-cell volumes from the EoSs with the parameters as determined from the fits, the volumes at $P = 6.15$ corresponds to 331.08 and 331.09 $Å^3$, which can be considered as identical with respect to mean experimental uncertainty (≈0.024 $Å^3$) in the volume determination in this study here.

4. Discussion

The investigations clearly reveal the existence of a structural transition, which is second-order from thermodynamical point of view, proper ferroelastic, and displacive in nature as manifested by the in-situ structure investigations. Considering the pure framework composed of octahedral and tetrahedral units around the Fe and S atoms, the framework topology remains unchanged with respect to local coordination within the building units. This is also proven to the extent that the main bands in the vibrational spectra remain virtually unchanged over the critical pressure within the experimentally accessible pressure range. There is no change of the number of modes, which are assigned to the tetrahedral SO_4 group, nor any splitting or any indication for a shoulder. This can be attributed to the fact that in both polymorphic forms the atoms occupy only a single crystallographic site and the geometry of the SO_4 group remains almost unaffected. The only discernible changes in the lattice-related regions of the spectra are found in those lattice modes attributable to octahedral vibrations. This can be explained that the weak new bands occurring in the Raman spectra beyond 6.15 GPa are a consequence, that the Fe atoms in the octahedra in the high-pressure form are distributed on two very similar but crystallographically independent sites.

As the dominating framework of the structure and its topology are virtually unchanged, one can easily understand the lack of any volume discontinuity and hence, why the transition definitely is not first order in nature. The fact that the compressibility of the two phases is very similar also shows that the structural differences between the two forms are not very large. Also, that in consequence the pressure dependencies of spectral band positions before or after P_c are extremely similar, there is an indication that the principal compression mechanisms are independent of the polymorphic form and their differences in symmetry. The accurate determination of the lattice constants with appropriate precision clearly proves the changes in the lattice metrics when the critical pressure value of 6.15 GPa is exceeded. The measurements clearly show a deviation from the monoclinic symmetry that can be assigned to the low-pressure polymorph. In addition, the structural investigations confirm the symmetry change from $C2/c$ to $P\bar{1}$ space-group symmetry on the basis of the measured diffraction intensities and the observed reflection conditions.

Comparing the results of the individual techniques used for the in-situ investigations here in this study, it is evident that the biggest change concerns the hydrogen-bond system originating from the molecular water. Regarding to the significant changes related to the band position of the $\tilde{\nu}_1$ O–H stretching band, it is evident that donor-acceptor distances and their evolution with pressure significantly change across the transition pressure. Following the empirical trend line as given by Libowitzky [70], the linear frequency shift towards lower frequencies at higher pressures corresponds to the expectation as the O···O contacts of hydrogen bonds decrease as the structure gets compressed. This is also confirmed by the structure investigations showing that the respective Ow···O1 and Ow···O2 distances get reduced from 3.24 to 3.05 Å and from 2.76 to 2.65 Å as determined close to the critical pressure at 5.5 GPa. At the transition pressure, the frequencies determined for the $\tilde{\nu}_1$(OH) band components are shifted towards higher wavenumbers, which corresponds to an increase of the respective O···O distance. The results of the structure investigations show that each of the O···O distances splits into two independent ones, with apparently very significant differences for the length of the hydrogen bridges (e.g. Ow···O1 splitting into values of 3.15 Å and 2.84 Å for Ow···O1A and Ow···O1B). In particular the role of the O1 acceptor atoms is remarkable, as the positional shifts cause O1B to take an enhanced role as acceptor, while O1A loses its equivalent role. In this context, a clear asymmetry in the binding system can be seen with the formation of a bifurcated Ow::O2B/O1B bridge on the one hand, and with the formation of a conventional bridging bond with O2A as a singular acceptor on the other hand (see Fig. 6).

According to Brown [71] repulsion arises for oxygen acceptor to donor distances below 2.7 Å. Nazzareni et al. [62] observed for gypsum that the repulsion becomes so strong and that the compression mechanism changes, giving rise to a structural phase transition. Approaching the phase transition the Ow-O2 distance decreases reaching a value as low as 2.651(4) Å at 5.50 GPa in $Fe SO_4{\cdot}H_2O$. The splitting of the O2 and O1 in the $C2/c$ structure into each two position in $P\bar{1}$ (i.e. O1A, O1B, O2A, and O2B) allows the independent rotation of the $FeAO_6$ octahedra relative to the $FeBO_6$ octahedra. In order to keep a better balance on the bond strengths for the Ow atoms, the possibility for independent atomic shifts decoupled from symmetry constraints allow the relative compressibilities to get adopted. Hence the stronger compression of Ow···O1B is compensated by keeping the distance Ow···O1A long, and simultaneously significantly shortening Ow···O2A opposes a relatively small change of Ow···O2B.

The changes in the role of the O1 and O2 oxygen atoms is related to small cooperative tiltings of the SO_4 tetrahedra and, in consequence, of the two individual adjacent FeO_6 octehadra. Due to the fact that the sulfate group is no more located on a diad, the tetrahedra have the freedom to be tilted off the former two-fold axis. Since the four O···O contacts, which are crucial for hydrogen bonding, orient each more or less within the a-b plane, it is not surprising that the strongest effects in

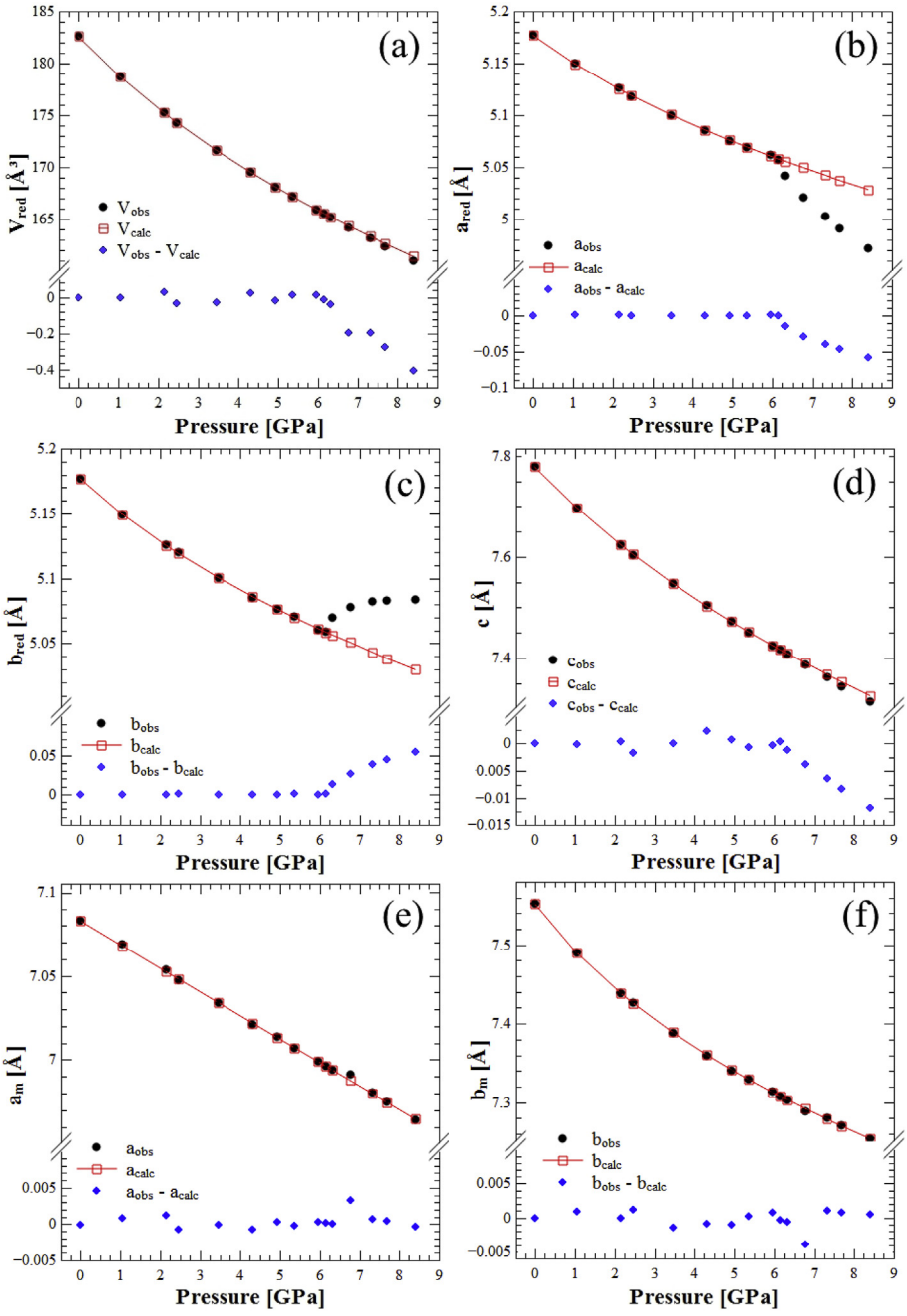

Fig. 8. Pressure evolution of the unit-cell parameters of $FeSO_4{\cdot}H_2O$: (a) unit-cell volume V, (b + c) lattice parameters a and b of the reduced cell, (d) lattice parameter c (=c_m). (e + f) lattice parameters a_m and b_m of the monoclinic $C2/c$ cell. Plots correspond to the data provided in Table 4. Red lines correspond to fits of BM-3 EoS with the respective parameters as quoted in Table 5. Blue symbols represent the deviations of the measured data points from the fits. (For interpretation of the references to color in this figure legend, the reader is referred to the Web version of this article.)

the lattice distortion affect the related lattice directions. This coincides with the evolution of the a_{red} and b_{red} directions of the reduced cell and the shortening of a_{red} (Fig. 8b) and the elongation of b_{red} (Fig. 8c) relative to the extrapolated vector lengths in the monoclinic phase directly matches the shortening of Ow···O1B while keeping Ow···O1A inactive in the role as an acceptor oxygen. The monoclinic-to-triclinic distortion of the lattice within this preferred plane direction apparently originate from the relative positional shifts of O1A and O1B atoms. The c-axis direction, which corresponds to the direction of corner sharing $[Fe O_4(H_2O)]^{6-}$ chains, provides evidence for a subtle, about 5 fold smaller compared to the a_{red} and b_{red} direction, change when crossing the critical transition point as confirmed by evolution of normalized pressure as a function of finite Eulerian strain (Fig. 9b).

5. Conclusions

We conclude that the high-pressure polymorph of ferrous sulfate monohydrate is unlikely to exist in the interior of giant Jovian icy satellites, since the maximum pressure to which hydrated sulfate minerals are exposed inside the icy mantles of these bodies do not exceed 5 GPa [18]. However, we do not suspect pure endmember $FeSO_4{\cdot}H_2O$ to occur in the icy mantle rather than Mg-dominated solid solutions between $MSO_4{\cdot}H_2O$ with M = Mg, Fe, Ni, Mn as interfered from chemical analysis of sulfate minerals in primitive chondrites [72]. Meusburger et al. [73] and Ende et al. [74] reported analogous $C2/c$ to $P\bar{1}$ phase transition for $MgSO_4{\cdot}H_2O$ at a critical pressure of transformation of 2.7 GPa. Given the large difference in the transition pressures we suggest that incorporation of even small amounts of Fe into the kieserite-type structure could

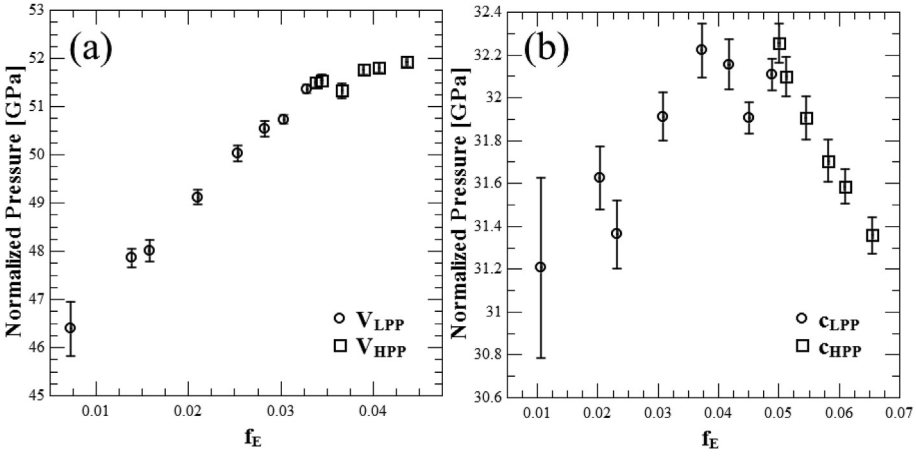

Fig. 9. Normalized pressure versus Eulerian strain in $FeSO_4{\cdot}H_2O$ as determined from (a) the experimental volume and (b) the *c*-lattice parameter. Both plots reveal discontinuous behaviour after the critical pressure of transformation as indicated by different trends for the low-pressure and the high-pressure polymorph.

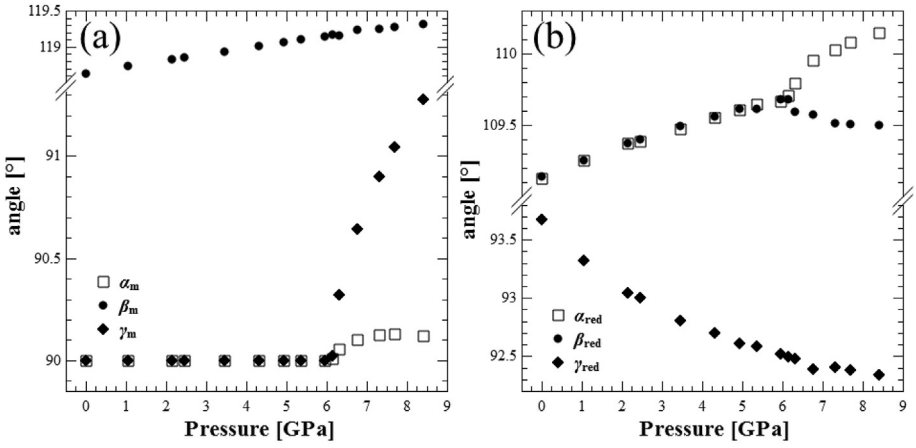

Fig. 10. Pressure evolution of the lattice angles α, β, γ in $FeSO_4{\cdot}H_2O$ in the setting of (a) the monoclinic *C*2/*c* cell (α_m~90°, β_m, γ_m~90°) and (b) the reduced cell ($\alpha_{red} \approx \beta_{red}$, γ_{red}) as shown in Fig. 5.

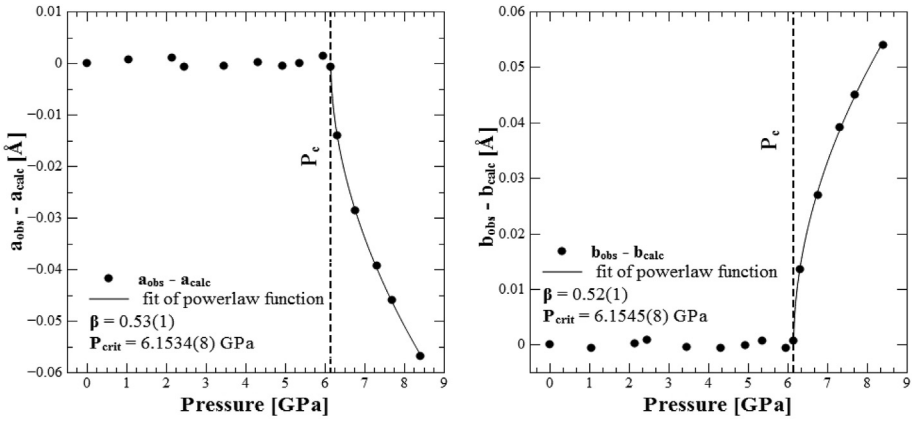

Fig. 11. Order-parameter analyses for the lattice directions *a* and *b* (of the reduced cell) in $FeSO_4{\cdot}H_2O$ corresponding to the evolution of their values as shown in Fig. 8b and c. The data points plot the differences of the observed values for the lattice constants of *a*- and *b*-axis in relationship to the calculated values as obtained from the EoS parameters for the monoclinic *C*2/*c* phase below 6 GPa (red symbols in Fig. 8b and c). The differences $\Delta_{o\text{-}c} = a_{obs}\text{-}a_{calc}$ and $b_{obs}\text{-}b_{calc}$ follow the power law $\Delta_{o\text{-}c} \propto |P\text{-}P_c|^{\beta}$ with β being the critical exponent, being ~0.50 as typical for second-order phase transitions. Solid lines correspond to the fits with the parameters as stated below.

significantly shift the transformation pressure towards higher pressures and hence extend the stability field of monoclinic kieserite in the interior of giant icy satellites. Moreover, our results are of great interest from a crystallochemical point of view since the unit-cell volume, lattice parameters and bonding lengths for $MgSO_4{\cdot}H_2O$ deviate significantly from isostructural transition metal compounds [25,30]. Deviation of the Mg end-member within this series of isostructural phases is not restricted to kieserite-type compounds but has been observed for numerous series of hydrated sulfates (i.e., the bloedite-type: $Na_2M(II)SO_4)_2 \cdot 4H_2O$ [75] and Tutton's salts: $K_2M(II)(SO_4)_2 \cdot 6H_2O$ [76]) and is also known for the selenate analogous series of the kieserite-type $M(II)SeO_4 \cdot H_2O$ [29]. The kieserite-type series appears to be a suitable testbed to study the influence of the aberrant behaviour of the magnesium end-member on comparative high-pressure structure-property relations.

Acknowledgments

Financial support through the Austrian Science Fund FWF (grant P 29149-N29 to MW) and the start-up funding of the University of Vienna (grant BE532003 to RM) are gratefully acknowledged. Furthermore, we want to thank the two anonymous reviewers for their careful reading and valuable comments which significantly improved the scientific quality of the manuscript.

References

[1] C.J. Fritzsche, Über eine neue Verbindung der schwefelsauren Talkerde mit Wasser, Ann. Phys. 118 (1837) 577–580.
[2] A.D. Fortes, I.G. Wood, M.J. Gutmann, $MgSO_4{\cdot}11H_2O$ and $MgCrO_4{\cdot}11H_2O$ based on time-of-flight neutron single-crystal Laue data, Acta Crystallogr. C 69 (2013a) 324–329.
[3] A.D. Fortes, K.S. Knight, I.G. Wood, Structure, thermal expansion and incompressibility of $MgSO_4{\cdot}9H_2O$, its relationship to meridianiite ($MgSO_4{\cdot}11\ H_2O$) and possible natural occurrences, Acta Crystallogr. B 73 (2017a) 47–64.
[4] A.D. Fortes, F. Fernandez-Alonso, M.G. Tucker, I.G. Wood, Isothermal equation of state and high-pressure phase transitions of synthetic meridianiite ($MgSO_4{\cdot}11D_2O$) determined by neutron powder diffraction and quasielastic neutron spectroscopy, Acta Crystallogr. B 73 (2017b) 33–46.
[5] R.C. Peterson, R. Wang, Crystal molds on Mars: melting of a possible new mineral species to create Martian chaotic terrain, Geology 34 (2006) 957–960.
[6] A.D. Fortes, K.S. Knight, A.S. Gibbs, I.G. Wood, Crystal structures of $NiSO_4{\cdot}9H_2O$ and $NiSO_4{\cdot}8H_2O$; magnetic properties, solid solutions and stability with respect to morenosite ($NiSO_4{\cdot}7H_2O$), Phys. Chem. Miner. 45 (2018) 695–712.
[7] A.D. Fortes, F. Browning, I.G. Wood, Cation substitution in synthetic meridianiite ($MgSO_4{\cdot}11H_2O$) II: variation in unit-cell parameters determined from X-ray powder diffraction data, Phys. Chem. Miner. 39 (2012b) 443–454.
[8] A.D. Fortes, I.G. Wood, K. Hudson-Edwards, M.J. Gutmann, Partitioning of Co^{2+} and Mn^{2+} into meridianiite ($MgSO_4{\cdot}11H_2O$): ternary solubility diagrams at 270 K; cation site distribution determined by single-crystal time-of-flight neutron diffraction and density functional theory, Fluid Phase Equilib. 437 (2017c) 1–13.
[9] A.D. Fortes, F. Browning, I.G. Wood, Cation substitution in synthetic meridianiite ($MgSO_4{\cdot}11H_2O$) I: X-ray powder diffraction analysis of quenched polycrystalline aggregates, Phys. Chem. Miner. 39 (2012a) 419–441.
[10] J.M. Powers, G.R. Buchanan, L. Adix, S. Zhang, A. Gao, T.L. McCavit, Effect of low-dose ferrous sulfate vs iron polysaccharide complex on hemoglobin concentration in young children with nutritional iron-deficiency anemia: a randomized clinical trial, J. Am. Med. Assoc. 317 (2017) 2297–2304.
[11] A. Alvarez-Fernandez, P. Garcıa-Laviña, J. Fidalgo, A. Abadia, A. Abadia, Foliar fertilization to control iron chlorosis in pear (Pyrus communis L.),, Trees Plant Soil 263 (2004) 5–15.
[12] K.A. Hudson Edwards, C. Schell, M.G. Macklin, Mineralogy and geochemistry of alluvium contaminated by metal mining in the Rio Tinto area, southwest Spain, Appl. Geochem. 14 (1999) 1015–1030.
[13] K.A. Hudson Edwards, Sources, mineralogy, chemistry and fate of heavy metal-bearing particles in mining-affected river systems, Mineral. Mag. 67 (2003) 205–217.
[14] K.M. Pitman, E.Z. Noe Dobrea, C.S. Jamieson, J.B. Dalton III, W.J. Abbey, E.C.S. Joseph, What lurks in the martian rocks and soil? Investigations of sulfates, phosphates, and perchlorates, reflectance spectroscopy and optical functions for hydrated Fe-sulfates, Am. Mineral. Vol. 99 (2014) 1593–1603.
[15] J.B. Dalton, O. Prieto-Ballestros, J.S. Kargel, C.S. Jamieson, J. Jolivet, R. Quinn, Spectral comparison of heavily hydrated salts with disrupted terrains on Europa, Icarus 177 (2005) 472–490.
[16] T.B. McCord, G.B. Hansen, D.L. Matson, Hydrated salt minerals on Europa's surface from the Galileo near-infrared mapping spectrometer (NIMS) investigation, J. Geophys. Res. 104 (1999) 11827–11851.
[17] T.B. McCord, G.B. Hansen, C.A. Hibbits, Hydrated salt minerals on Ganymede's surface: evidence of an ocean below, Science 292 (2001a) 1523–1525.
[18] E.L. Gromnitskaya, O.F. Yagafarov, A. Gennadievich Lyapin, V. Brazhin, I.G. Wood, M.G. Tucker, A.D. Fortes, The high-pressure phase diagram of synthetic epsomite ($MgSO_4{\cdot}7H_2O$ and $MgSO_4{\cdot}7D_2O$) from ultrasonic and neutron powder diffraction measurements, Phys. Chem. Miner. 40 (2013) 271–285.
[19] W. Wang, A.D. Fortes, D.P. Dobson, C.M. Howard, J. Bowles, N.J. Hughes, I.G. Wood, Investigation of high-pressure planetary ices by cryo-recovery. II. High-pressure apparatus, examples and a new high-pressure phase of $MgSO_4{\cdot}5H_2O$, J. Appl. Crystallogr. 51 (2018) 692–705.
[20] S.J. Chipera, D.T. Vaniman, Experimental stability of magnesium sulfate hydrates that may be present on Mars, Geochem. Cosmochim. Acta 71 (2007) 241–250.
[21] T.B. McCord, T.M. Orlando, T. Gleen, G.B. Hansen, M.T. Sieger, N.G. Petrik, L. Van Keulen, Thermal and radiation stability of the mineals epsomite, mirabilite and natron under Europa environmental condtions, J. Geophys. Res. 106 (2001b) 3311–3319.
[22] T. Wang, K.A. Debelak, J. Roth, Dehydration of iron(II) sulfate heptahydrate, Thermochim. Acta 462 (2007) 89–93.
[23] A. Wang, J.J. Freeman, B.L. Jolliff, Phase transition pathways of the hydrates of magnesium sulfate in the temperature range 50°C to 5°C: implication for sulfates on Mars, J. Geophyiscal Res. 114 (2009) E04010 1–E0401028.
[24] J. Leonhardt, R. Weiss, Das Kristallgitter des Kieserits $MgSO_4 \cdot H_2O$, Naturwissenschaften: Kurze Orginalmitteilungen 44 (1957) 338–339.
[25] M. Wildner, G. Giester, The crystal structures of kieserite-type compounds. I. Crystal structures of $Me(II)SO_4{\times}H_2O$ [Me=Mn, Fe, Co, Ni, Zn], Neues Jahrbuch Mineral. Monatsh. 296–306 (1991).
[26] W.H. Baur, Über Kristallstrukturelle Beziehungen zwischen Amblygonit, Kieserit und Titanit, Beiträge zur Mineralogie und Petrographie 6 (1959) 399–404.
[27] F.C. Hawthorne, L.A. Groat, M. Raudsepp, T.S. Ercit, Kieserite, $Mg(SO_4)(H_2O)$, A titanite-group mineral, Neues Jahrbuch Mineral. Abhand. 157 (1987) 121–132.
[28] J. Zemann, Die Strukturtypen des Lazuliths, Lipscombits, Caminits und Kieserits: eine Gruppe topologisch eng verwandter Atomanordnungen, Aufschluss 41 (1990) 7–11.
[29] G. Giester, M. Wildner, The crystal structures of kieserite-type compounds. II. Crystal structures of $Me(II)SeO_4 \cdot H_2O$ (Me = Mg, Mn, Co, Ni, Zn), Neues Jahrbuch Mineral. Monatsh. 3 (1992) 135–144.
[30] A. Bechtold, M. Wildner, Crystal chemistry of the kieserite-cobaltkieserite solid solution, $Mg_{1-x}Co_x(SO_4) \cdot H_2O$: well behaved oddities, Eur. J. Mineral. 28 (2016) 43–52.
[31] D. Talla, M. Wildner, Investigation of the kieserite–szomolnokite solid solution series, $(Mg,Fe)SO_4{\cdot}H_2O$, with relevance to Mars: a study on crystal chemistry, FTIR- and Raman-spectroscopy under ambient and Martian temperature conditions, Am. Mineral. (2019). Submitted for publication.
[32] B. Rieck, G. Giester, Voudourisite, IMA 2012-042, CNMNC Newsletter 14, 2012, p. 1287.
[33] B. Rieck, C.L. Lengauer, G. Giester, Voudourisite, $Cd(SO_4){\cdot}H_2O$, and Lazaridisite, $Cd_3(SO_4)_3{\cdot}8H_2O$, Two New Minerals from the Lavrion Mining District., Greece, Mineralogical Magazine, 2018, pp. 1–31. https://doi.org/10.1180/mgm.2018.157.
[34] J.M. Bregeault, P. Herpin, Crystal structure of $CdSO_4.H_2O$, Bull. Soc. Fr. Mineral. Cristallogr. 93 (1970) 37–42.
[35] G. Giester, The crystal structures of $CuSO_4 \cdot H_2O$ and $CuSeO_4 \cdot H_2O$, and their relationships to kieserite, Mineral. Petrol. 38 (1988) 277–283.
[36] G. Giester, C.L. Lengauer, G. Redhammer, Charcterisation of the $FeSO_4 \cdot H_2O$ - $CuSO_4 \cdot H_2O$ solid solution series, and the nature of poitevinite, $(Cu,Fe)SO_4 \cdot H_2O$, Can. Mineral. 32 (1994) 873–884.
[37] C.L. Lengauer, G. Giester, Rietveld refinement of the solid-solution series: $(Cu,Mg)SO_4{\cdot}H_2O$, Powder Diffr. 10 (1995) 189–194.
[38] J. Emsley, Very strong hydrogen bonding, Chem. Soc. Rev. 9 (1980) 91–124.
[39] C.H. Chio, S.K. Sharma, D.W. Muenow, The hydrates and deuterates of ferrous sulfates ($FeSO_4$): a Raman spectroscopic study, J. Raman Spectrosc. 38 (2007) 87–99.
[40] H. Binder, Lexikon der chemischen Elemente: Das Periodensystem in Fakten, Daten und Zahlen., 1, Auflage, 1999.
[41] R. Miletich, D.R. Allan, W.F. Kuhs, High-pressure single-crystal techniques, Rev. Mineral. Geochem. 41 (2000) 445–519.
[42] R. Boehler, K. De Hantsetters, New anvil designs in diamond cells, High Press. Res. 24 (2004) 391–396.
[43] S. Klotz, J.C. Chervin, P. Munsch, G. Le Marachand, Hydrostatic limits of 11 pressure transmitting media, J. Phys. D: Appl. Phys. 42 (2009).
[44] G.J. Piermarini, S. Block, J.S. Barnett, Hydrostatic limits in liquids and solids up to 100 kbar, J. Appl. Phys. 44 (1973) 5377–5382.
[45] D. Errandonea, Y. Meng, M. Somayazulu, D. Häusermann, Pressure-induced $\alpha{\rightarrow}\omega$ transition in titanium metal: a systematic study of the effects of uniaxial stress, Phys. B Condens. Matter 355 (2005) 116–125.
[46] K.S. Scheidl, A. Kurnosov, D.M. Trots, T. Boffa Ballaran, R.J. Angel, R. Miletich, Extending the single-crystal quartz pressure gauge up to hydrostatic pressure of 19 GPa, J. Appl. Crystallogr. 49 (2016) 2129–2137.
[47] S.D. Jacobson, C.M. Holl, K.A. Adams, Compression of single-crystal magnesium oxide to 118 GPa and a ruby pressure gauge for helium pressure media, Am. Mineral. 93 (2008) 1823–1828.
[48] R.J. Angel, J. Gonzalez-Platas, *ABSORB-7* and *ABSORB-GUI* for single-crystal absorption corrections, J. Appl. Crystallogr. 46 (2013) 252–254.
[49] C.B. Hübschle, G.M. Sheldrick, B. Dittrich, ShelXle, A graphical user interface for *SHELXL*, J. Appl. Crystallogr. 44 (2011) 1281–1284.
[50] G.M. Sheldrick, A short history of SHELX, Acta Crystallogr. 64 (2008) 112–122.
[51] I.D. Brown, R.D. Shannon, Empirical bond-strength-bond-length curves for oxides, Acta Crystallogr. A29 (1973) 266–282.
[52] J. Gonzalez-Platas, M. Alvaro, F. Nestola, R. Angel, EosFit7-GUI, A new graphical user interface for equation of state calculations, analyses and teaching, J. Appl. Crystallogr. 49 (2016) 1377–1382.
[53] H.E. King, L.W. Finger, Diffracted beam crystal centring and its application to high-pressure crystallography, J. Appl. Crystallogr. 12 (1979) 374–378.
[54] F. Birch, Finite elastic strain of cubic crystals. Phys. Rev. Vol. 71 (1947) 809–824.
[55] R.J. Angel, Win_Strain 4.11, 2011. http://www.rossangel.com/text_strain.htm.
[56] A.D. Fortes, I.G. Wood, M. Alfredsson, L. Vočadlo, K.S. Knight, The thermoelastic properties of $MgSO_4{\cdot}7D_2O$ (epsomite) from powder neutron diffraction and ab initio calculation, Eur. J. Mineral. 18 (2006a) 449–462.
[57] A.D. Fortes, H.E.A. Brand, L. Vočadlo, A. Lindsay-Scott, F. Fernandez-Alonso, I.G. Wood, P-V-T equation of state of synthetic mirabilite ($Na_2SO_4{\cdot}10D_2O$) determined by powder neutron diffraction, J. Appl. Crystallogr. 46 (2013b) 448–460.
[58] P. Comodi, S. Nazzareni, T. Balic-Zunic, A. Zucchini, M. Hanfland, The high-pressure behaviour of bloedite: a synchrotron single-crystal X-ray diffraction study, Am. Mineral. 99 (2014) 511–518.
[59] P. Comodi, S. Nazzareni, T. Balic-Zunic, A. Zucchini, M. Hanfland, The compression behaviour of blödite at low and high temperature up to ~10 GPa: implications for

the stability of hydrous sulfates on icy planetary bodies, Icarus 285 (2017) 137–144.
[60] S. Nazzereni, P. Comodi, M. Hanfland, High-pressure single-crystal synchrotron X-ray diffraction of kainite ($KMg(SO_4)Cl\ 3H_2O$), Phys. Chem. Miner. 45 (2018).
[61] P. Comodi, S. Nazzareni, P.F. Zanazzi, S. Speziale, High-pressure behaviour of gypsum: a single crystal X-ray study, Am. Mineral. 93 (2008) 1530–1537.
[62] S. Nazzereni, P. Comodi, L. Bindi, L.S. Dubrovinsky, The crystal structure of gypsum-II determined by single-crystal synchrotron X-ray diffraction data, Am. Mineral. 95 (2010) 655–658.
[63] J. Haines, J.M. Léger, C. Chateau, R. Bini, L. Ulivi, Ferroelastic phase transition in rutile-type germanium dioxide at high pressure, Phys. Rev. B 58 (1998) 2909–2912.
[64] Y. Tsuchida, T. Yagi, A new, post-stishovite highpressure polymorph of silica, Nature 340 (1989) 217–220.
[65] J. Buchen, H. Marquardt, K. Schulze, S. Speziale, T. Boffa Ballaran, N. Nishiyama, M. Hanfland, Equation of state of polycrystalline stishovite across the tetragonal-orthorhombic phase transition, J. Geophys. Res. B Solid Earth 123 (2018) 7347–7360.
[66] L.S. Dubrovinsky, A.B. Belonoshko, Pressure-induced phase transition and structural changes under deviatoric stress of stishovite to $CaCl_2$-like structure, Geochem. Cosmochim. Acta 60 (1996) 3657–3663.
[67] K.J. Kingma, R.E. Cohen, R.J. Hemley, H.K. Mao, Transformation of stishovite to a denser phase at lowermantle pressures, Nature 374 (1995) 243–246.
[68] D. Errandonea, Landau theory applied to phase transitions in calcium orthotungstate and isostructural compounds, Europhys. Lett. 77 (2007) 56001–56006.
[69] D. Errandonea, F.J. Manjón, On the ferroelastic nature of the scheelite-to-fergusonite phase transition in orthotungstates and orthomolybdates, Mater. Res. Bull. 44 (2009) 807–811.
[70] E. Libowitzky, Correlation of O-H stretching frequencies and O-H…O hydrogen bond lengths in minerals. Monatshefte Chem. Vol. 130 (1999) 1047–1059.
[71] I.D. Brown, On the geometry of the O-H…O hydrogen bonds, Acta Crystallogr. A32 (1976) 23–31.
[72] K. Frederikson, J.F. Kerridge, Carbonates and Sulfates in CI Chondrites., Formation by Aqueous Activity on the Parent Body, Meteoritics vol. 23, 1988, pp. 35–44.
[73] J.M. Meusburger, M. Ende, D. Talla, R. Miletich, M. Wildner, Pressure induced second order phase transition in monohydrated magnesium sulfate ($MgSO_4{\cdot}H_2O$): a new polymorph potentially occurring on icy satellites.,, Geophys. Res. Abstr. Vol. 20 (2018) 2018. EGU2018-8136, EGU General Assembly.
[74] M. Ende, J. Meusburger, D. Talla, R. Miletich, M. Wildner, First evidence of a displacive transformation in $MgSO_4xH_2O$ under high pressures, in: Zeitschrift für Kristallographie, Supplement Issue 38, 26th Annual Meeting of the German Crystallographic Society (DGK), Essen, Germany, 5-8 March vol. 81, 2018.
[75] D. Stoilova, M. Wildner, Bloedite type compounds $Na_2Me(SO_4)_2{\cdot}4H_2O$ (Me= Mg, Co, Ni, Zn): crystal structure and hydrogen bonding systems, J. Mol. Struct. 706 (2004) 57–63.
[76] F. Bosi, G. Berlardi, P. Ballirano, Structural features in Tutton's salt $K_2([M^{2+}(H_2O)_6](SO_4)_2$, with M^{2+} = Mg, Fe, Co, Ni ,Cu and Zn, Am. Mineral. 94 (2009) 74–82.